Journal of Solid State Chemistry 183 (2010) 2602–2608

Contents lists available at ScienceDirect

Journal of Solid State Chemistry

journal homepage: www.elsevier.com/locate/jssc

Infrared spectroscopic study of the local structural changes across the metal insulator transition in nickel-doped $GdBaCo_2O_{5.5}$

P. Yasodha, M. Premila *, A. Bharathi, M.C. Valsakumar, R. Rajaraman, C.S. Sundar

Materials Science Group, Indira Gandhi Centre for Atomic Research, Kalpakkam 603 102, India

ARTICLE INFO

Article history:
Received 13 May 2010
Received in revised form
9 August 2010
Accepted 1 September 2010
Available online 8 September 2010

Keywords:
Infrared spectroscopy
Layered perovskites
Metal–insulator transition

ABSTRACT

Phonons in $GdBaCo_2O_{5.5}$ have been identified using infrared spectroscopy and their mode assignments have been carried out using ab initio lattice dynamical calculations. Metal insulator transitions in undoped and nickel-doped $GdBaCo_2O_{5.5}$ have been probed using infrared absorption spectroscopy. The phonon modes corresponding to the bending mode of the CoO_6 octahedra/pyramids are seen to soften, broaden and develop an asymmetry across the insulator–metal transition pointing to extensive electron phonon interaction effects in these systems. Correlated changes of the phonon line shape parameters associated with the transition indicate a suppression of T_{MIT} with increased nickel doping of the cobalt sublattice. Temperature dependence of the octahedral stretching mode frequencies in undoped $GdBaCo_2O_{5.5}$ points to distinct structural distortions accompanying the high temperature metallic transition.

1. Introduction

Cobalt containing oxides have attracted considerable attention in recent years due to a unique combination of their electrical and magnetic properties [1–6]. In particular oxygen deficient layered perovskites of the formula $LnBaCo_2O_{5+\delta}$ present a rich phase diagram exhibiting a variety of electrical, magnetic and structural transitions as a consequence of the interplay of spin, charge and orbital degrees of freedom [7–11]. The crystal structure of these compounds consists of a sequence of $[CoO_2]$–$[BaO]$–$[CoO_2]$–$[LnO_{0.5}]$–$[CoO_2]$ layers along the crystallographic '*c*' direction (inset of Fig. 1a) [11–13]. The oxygen content in these compounds plays a very crucial role in determining its transport and magnetic properties [14] (Table 1), since this dictates the nominal valence state of cobalt (varying from +3.5 for $\delta=1$ to +2.5 for $\delta=0$). For $\delta=0.5$ where only Co^{3+} ions are present, the oxygen ions in the Ln–O layers order into alternating filled and empty rows running along the '*b*' axis leading to alternating octahedral and pyramidal environment for the cobalt ions [13,14]. The large diversity in properties of these systems is primarily associated with the fact that cobalt exhibits multiple spin states—low spin (LS, $t_{2g}^6\ e_g^0$), intermediate spin (IS, $t_{2g}^5\ e_g^1$) and high spin (HS, $t_{2g}^4\ e_g^2$) states, in addition to the variety of stable oxidation states (Co^{2+}, Co^{3+} and Co^{4+}), thus adding to the complexity of the phase diagram [13–17]. At low temperatures, the LS and IS states are energetically favoured, while an increase in temperature favours the LS–IS and IS–HS transitions [18–20].

These materials exhibit several magnetic transitions in addition to metal–nonmetal transitions [11–14] (Table 1). This metal-insulator transition (MIT) in $LnBaCo_2O_{5.5}$ has been a subject of considerable interest, the origin of which still remains unresolved [11–14,18–24]. A few reports are suggestive of a magnetic origin to this MIT, wherein a thermally induced spin state transition of the Co^{3+} ion from the LS/IS to the HS states is responsible for the transition to the metallic state [12,13,19–22]. While neutron diffraction measurements across the transition indicate that the low temperature insulating phase arises as a consequence of the ordering of the e_g orbitals [25], studies based on the O-isotope effect on the transition temperature (T_{MIT}) [26] suggested the presence of lattice polarons that could localize the electrons and hence provided an alternative picture of this transition. Recently high resolution synchrotron measurements have revealed a structural transformation accompanying the MIT [27]. $GdBaCo_2O_{5.5}$ is known to exhibit a metal to insulator transition (MIT) at $\sim$370 K, a paramagnetic to ferromagnetic transition at 270 K and ferromagnetic to antiferromagnetic transition at 240 K [18].

Chemical substitution of the cobalt sublattice in $GdBaCo_2O_{5.5}$ with nickel—an electron dopant is seen to modify the transport and magnetic behavior of this compound [23]. It is observed that the room temperature resistivity of the parent material decreases systematically, with increased nickel content and in addition a clear suppression of the T_{MIT} was also observed [23,24]. It was interesting to note that the variation in T_{MIT} with nickel substitution correlated well with the orthorhombic distortion,

* Corresponding author. Fax: +91 44 27480081.
E-mail address: premila@igcar.gov.in (M. Premila).

0022-4596/$ - see front matter © 2010 Elsevier Inc. All rights reserved.
doi:10.1016/j.jssc.2010.09.003

possibly pointing to a structural link of the MIT [23] wherein these distortions are expected to modify the crystal field splitting energies, leading to the observed delocalised state.

Although a large body of studies have focused on transport and magnetic properties [12,13,21–24,28], across the MIT, it is well known that optical methods such as infrared or Raman spectroscopy have proved to be valuable in trying to understand the nature of these transitions in related systems [29–34].

In the present work we have carried out infrared spectroscopic studies to look for the interplay between MIT and the structural aspects. Far infrared absorption spectroscopic measurements were carried out on the layered double perovskite $GdBaCo_2O_{5.5}$ in the range 125–650 cm^{-1} and the infrared active phonon modes have been identified for the first time. Ab initio lattice dynamical calculations using VASP simulation program, were carried out in order to estimate the phonon frequencies that helped in mode assignments. We have also tried to obtain additional insights on the local structural changes associated with doping the cobalt sublattice with nickel on the phonon modes of the parent material. The present study largely focuses on using in situ variable temperature far infrared absorption spectroscopy to follow the phonon modes in both undoped and Ni-doped $GdBaCo_2O_{5.5}$ across the transition temperature, in an effort to understand the nature of this transition. Both the octahedral bending and the stretching modes have been followed across the transition temperature.

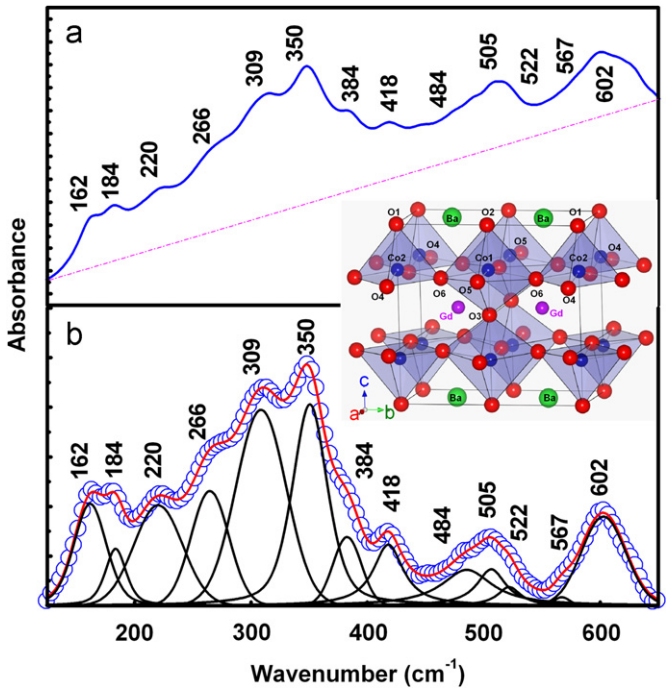

Fig. 1. (a) As recorded room temperature far infrared absorption spectrum of $GdBaCo_2O_{5.5}$ in the range 125–650 cm^{-1} and (b) background subtracted (a linear end to end background in the 125–650 cm^{-1} range has been subtracted) room temperature spectrum showing the fits in the 125–650 cm^{-1} range.

2. Experiment

Polycrystalline samples of $GdBaCo_2O_{5.5}$ and nickel-doped $GdBaCo_{2-x}Ni_xO_{5.5}$ (x=0.1, 0.2 and 0.4) were synthesized by the solid-state reaction method and characterized using X-ray diffraction measurements and ac susceptibility measurements [23]. Room temperature far infrared absorption measurements were carried out using a Bomem make DA8 FTIR spectrophotometer operating at a resolution of 4 cm^{-1}. Measurements in the far infrared range (125–650 cm^{-1}) have been carried out on all the above powder samples dispersed in cesium iodide matrix, using a combination of a Globar source, a 6 μm extended mylar beam splitter and a DTGS detector. Temperature variation (450–77 K) was achieved using an Oxford make continuous flow cryostat integrated with a pump, a gas flow meter and an Oxford make ITC temperature controller.

3. Results and discussion

3.1. Infrared active phonons in $GdBaCo_2O_{5.5}$ and their assignments

Fig. 1a shows the experimentally observed room temperature spectrum of $GdBaCo_2O_{5.5}$ recorded in the far infrared region covering the 125–650 cm^{-1} range. A linear background spanning

Table 1
Summary of various dopings and related magnetic, electrical and structural transitions.

System	Magnetic T_c;T_N	Electrical T_{MIT}	Structure	Reference
$GdBaCo_2O_{5+x}$				Ref. [14]
$x=0$	AF	Insulator	Tetragonal	
$0<x<0.45$	T_c=250–275 K	Insulator	Tetragonal	
$0.45<x<0.55$	T_c=280–260 K T_N=180–250 K	340–360 K	Orthorhombic	
$x>0.55$	$T_c<150$ K $T_N<100$ K	<100 K	Orthorhombic+Tetragonal	
$GdBaCo_{2-x}Ni_XO_{5.5}$				
x=0–0.4	T_c=280–200 K	350–300 K	Orthorhombic (RT)	Ref. [23]
$Gd_{1-x}Ce_xBaCo_2O_{5.5}$				
x=0–0.1	T_c=270–215 K T_N=240–220 K		Orthorhombic (RT)	Solid State Communications **144** 215 (2005)
$GdBaCo_{2-x}Fe_xO_{5.5}$				
x=0–0.4	T_c=278–300 K	360–364 K	Orthorhombic (RT)	Yasodha et al. to be published
$Gd_{1-x}Ca_xBaCo_2O_{5.5}$				
x=0–0.25	T_c=278–316 K	Not measured	Orthorhombic (RT)	
$Gd_{1-x}Sr_xBaCo_2O_{5.5}$				
x=0–0.1	T_c=278–290 K	360 K	Orthorhombic (RT)	

the whole range end to end has been subtracted and all the discernable phonon modes in the whole range have been fitted and the mode frequencies extracted (Fig. 1b). The orthorhombic structure of $GdBaCo_2O_{5.5}$ belongs to the *Pmmm* space group symmetry and is represented by rows of pyramids and octahedra running along the '*a*' axis. The primitive cell contains two formula units having 19 atoms/unit cell [12,13,35]. Table 2 shows the crystallographic positions of the various atoms along with their coordinates [12,13]. The crysrallographic structure of $GdBaCo_2O_{5.5}$ showing the positions of each of the atoms in the unit cell is shown in the inset of Fig. 1a. Co1 and Co2 correspond to the cobalt in the octahedral and pyramidal positions. O6 from the 4u sites share octahedral and pyramidal sites, while O4 and O5 connect pyramids and octahedra along the '*a*' axis, respectively. O1 and O2 represent oxygen in the Ba–O plane while O3 represents the oxygen along the Gd–O planes.

Table 2
Crystallographic positions of $GdBaCo_2O_{5.5}$ at room temperature (from Refs. [12, 13]).

Atom	Crystallographic position	Position coordinates
Gd	2p	1/2, 0.2722, 1/2
Ba	2o	1/2, 0.25, 0
Co1	2r	0, 1/2, 0.2522
Co2	2q	0, 0, 0.2562
O1	1a	0, 0, 0
O2	1e	0, 1/2, 0
O3	1g	0, 1/2, 1/2
O4	2s	1/2, 0, 0.3132
O5	2t	1/2, 1/2, 0.2737
O6	4u	0,0.245, 0.2929

Factor group analysis predicts a total of 56 vibrational modes of which 32 modes are infrared (IR) active ($11B_{1u}+11B_{2u}+10B_{3u}$) and 24 ($8Ag+3B_{1g}+5B_{2g}+8B_{3g}$) are Raman active modes. Although theory predicts a total of 32 IR active modes, only 13 infrared active modes have been observed experimentally (Fig. 1). In an attempt to assign these modes, ab initio lattice dynamical calculations using VASP simulation package [36] have been carried out, with which the vibrational frequencies and their respective polarizations have been calculated at the Γ point in the Brillouin zone. The calculations were done using the spin polarized formalism and within the generalized gradient approximation [37]. The calculations were carried out in a plane wave basis with the pseudopotentials generated using the projector augmented wave (PAW) method [38]. A $8\times4\times4$ k grid Monkhost–Pack has been used for the Brillouin zone sampling and 500 eV for plane wave cutoff energy. The structure is optimized to minimize the forces on atoms. The Hessian matrix of the total energy with respect to the displacements is computed within density functional perturbation theory. The symmetry of the structure was exploited to reduce the number of computations of total energy of the displaced configurations to the bare minimum. The amplitude of displacements along the *x*, *y* and *z* directions for the atoms associated with each mode along with mode frequencies have been derived from eigen vectors and eigen values of Hessian matrix. Additional details of computational method and results will be published elsewhere [39]. Table 3 lists the computed IR active modes along with their symmetry and atoms showing significant displacements for each mode. Experimentally observed infrared modes along with their relative intensities are also listed in Table 3 for comparison. The amplitude of displacements along the *x*, *y* and *z* axis involving the various

Table 3
Comparison of experimentally observed phonon frequencies with theoretically estimated frequencies showing their symmetries and preliminary mode assignments. The relative intensities are indicated within brackets.

S. no	Mode symmetry	Infrared frequency (cm^{-1})		Atoms significantly involved in displacements	Dominant motions
		Computed	Experimental		
1	B_{1u}	616	602 (8.5%)	Co1, O3,O2	Co–O Stretch *c*-axis
2	B_{2u}	587		Co2, O3, O6	Co–O Stretch a–b plane
3	B_{1u}	553	567 (0.3%)	Co2,O6	Co–O Stretch a–b plane
4	B_{1u}	531	522 (1.4%)	Co2,Co1,O1,O2,O3	Co–O Stretch 'c' axis
5	B_{3u}	511	505 (3.3%)	Co1,O5,O6	Co–O Stretch a–b plane
6	B_{1u}	451	484 (5.6%)	Co2,O4,O6	Co–O Stretch a–b plane
7	B_{2u}	400	418 (5.8%)	Co1,Co2,O1,O2, O4,O5	Co–O–Co bending
8	B_{3u}	397	384 (4.3%)	Co2, Co1, O6,O4	Co–O–Co bending
9	B_{2u}	374		Co1, O3, O4, O5	Co–O stretch a–b plane
10	B_{3u}	334		C01, Co2, O4	Co–O–Co bending
11	B_{1u}	332	350 (18.3%)	Co1,Co2, O4,O5,O6	Co–O–Co bending
12	B_{1u}	327		Co2, O4, O5	Co–O Stretch a-b plane
13	B_{2u}	301	309 (21.5%)	Co2,O2,O3, O1	Co lattice mode
14	B_{2u}	297		Co1, O4, O5	Co lattice mode
15	B_{2u}	281		Gd, O6	Gd lattice mode
16	B_{3u}	263	266 (9.5%)	Ba,Co1,O1,O6	Ba lattice mode
17	B_{3u}	250		Co2, O1, O6	Co lattice mode
18	B_{3u}	233		Co2, O4	Co lattice mode
19	B_{1u}	216	220 (10.7%)	Co1,O3,O4,O5	Co lattice mode
20	B_{2u}	196		Co1, O4, O6	Co lattice mode
21	B_{1u}	168	184 (3.1%)	Gd, O4,O5,O6	Gd lattice mode
22	B_{2u}	161	162 (7.8%)	Co1,O2,O1	Co lattice mode
23	B_{3u}	155		Co1, Co2, O4, O6	Co lattice mode
24	B_{1u}	147		Co1, Co2, O4	Co lattice mode
25	B_{2u}	137		Ba, Co2, O3	Ba, Co lattice mode
26	B_{1u}	121		Ba, Co1, O3	Ba, Co lattice mode
27	B_{3u}	119		Ba,Co2, O4	Ba, Co lattice mode
28	B_{2u}	82		Gd, Ba, O1, O3	Gd, Ba lattice mode
29	B_{3u}	70		Gd, Ba, O1, O3	Gd, Ba lattice mode
30	B_{2u}	0.3		Gd, Ba, Co1, Co2	Acoustic mode
31	B_{3u}	1		Gd, Ba, Co1, Co2	Acoustic mode
32	B_{1u}	3		Gd, Ba, Co1, Co2	Acoustic mode

atoms for each calculated mode frequency have been derived from VASP calculations. Out of 32 IR active modes computed from VASP, 29 modes have nonzero frequencies and remaining three modes with $< 3\ cm^{-1}$ correspond to acoustic modes involving translational motions along x, y and z directions. Based on the magnitude of these displacements and also based on literature reports of related systems [20] the modes have been broadly assigned as indicated in Table 3. While the major high frequency phonons at 602 and 505 cm^{-1} are assigned to the Co–O stretching frequencies of the CoO_6 octahedra along the c-axis and the a–b plane, respectively, the modes in the range $300 < \nu < 420\ cm^{-1}$ are attributed to the O–Co–O bending modes of the CoO_6 octahedra/pyramids. It is to be mentioned at the outset that the stretching modes of the pyramids cannot be followed with confidence owing to their poor oscillator strengths and hence all changes in the stretching mode frequencies are hereby generally referred to as arising due to octahedral distortions. The low-frequency modes appearing at $\nu < 300\ cm^{-1}$ are related to the lattice modes. More detailed discussion about mode assignments along with computed IR intensities and Raman active modes can be found elsewhere [39].

3.2. Compositional dependence of phonons in $GdBaCo_2O_{5.5}$ on doping with nickel

Fig. 2a and b shows the set of far infrared spectra of both undoped and nickel-doped $GdBaCo_2O_{5.5}$ recorded at room temperature and at 77 K, respectively. As mentioned earlier the parent compound ($x=0$) exhibits 13 infrared active modes at room temperature (Fig. 1). Although no new modes are seen on doping with nickel, one can observe systematic changes in the phonon line shapes as one increases the nickel content at room temperature. The modes become progressively broader and less intense with increased nickel content. For higher dopant concentration ($x=0.2$ onwards) the modes are no longer resolvable and are observed to be totally submerged by the electronic absorption background. This observed variation in the phonon modes is consistent with the earlier resistivity measurements wherein Ni substitution at the Co site drastically affects the transport behavior of the system [23]. It is observed that the room temperature resistivity of the parent material decreases systematically with increased nickel content [23]. The observed smearing out of the phonon modes for increased dopant concentration can be understood as arising on account of the enhanced background absorption caused by an effective increase in the charge carriers in the delocalised state.

As regarding the variation in the phonon frequencies as a function of doping with nickel, it is evident from the set of spectra recorded at 77 K (the spectra of the samples at 77 K (Fig. 2b) are better resolved and are hence amenable for analysis), that while the low frequency modes $< 400\ cm^{-1}$ exhibit a marginal shift by less than a percent, the high frequency stretch modes exhibit interesting changes. The 624 cm^{-1} mode corresponding to the Co–O stretching vibration along the c-axis of the CoO_6 octahedra, is observed to drastically soften by about 14 cm^{-1} with increased nickel content, while the 515 cm^{-1} mode attributed to the Co–O stretching along the a–b plane is observed to harden by $\sim 5\ cm^{-1}$ (Fig. 3). This suggests a slight elongation of the CoO_6 octahedra along the c-axis accompanied by a marginal contraction along the a–b plane. It is to be mentioned here that lattice parameters deduced by XRD measurements also indicate an increase in the 'b' and 'c' axis lattice parameters, associated with a decrease along the 'a' axis [23]. The above observation points out to the fact that changes in lattice parameters as seen by XRD measurements are indeed associated with changes in the octahedral/pyramidal structural parameters. The variation of the orthorhombicity with Ni content that correlated well with the variation in T_{MIT} [23] is compared with the changes in the octahedral stretch frequencies as obtained from the present measurements (Fig. 3) providing additional proof for structural changes across the MIT in these systems. The increased orthorhombic distortion with increased nickel doping is expected to modify the crystal field splitting energies leading to decreased band gaps. It is also to be noted that the observed contraction along the a–b plane could mean a greater overlap of the oxygen p orbitals with the Co d orbitals leading to delocalization of the charge carriers, thus explaining the decreased resitivity observed on doping the parent material with nickel.

3.3. In situ variable temperature measurements

Fig. 4a shows a select set of as recorded high temperature far infrared spectra of $GdBaCo_2O_{5.5}$ in the range 300–400 K, spanning the T_{MIT} ($\sim$370 K). Room temperature spectrum exhibits sharp and highly resolved phonon features clearly indicative of the insulating nature of the sample. On increasing the temperature,

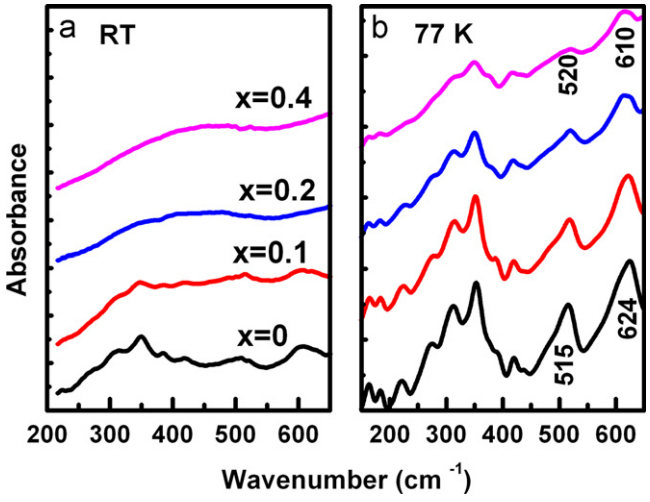

Fig. 2. Far infrared spectra of $GdBaCo_{2-x}Ni_xO_{5.5}$ ($x=0$, 0.1, 0.2 and 0.4) recorded at (a) 300 and (b) 77 K.

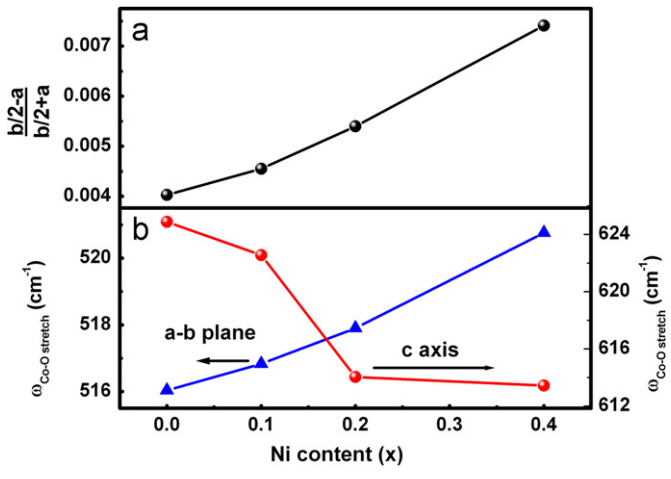

Fig. 3. (a) Variation of orthorhombicity as deduced by XRD and (b) variation of Co–O stretching frequencies of the CoO_6 octahedra along a–b plane and c-axis as a function of Ni content at 77 K. Note the correlation between the variation in the Co–O stretching frequencies and the orthorhombicity.

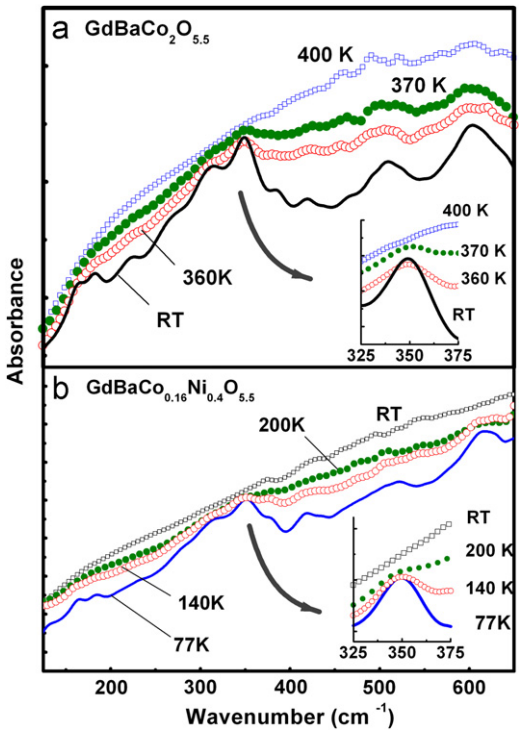

Fig. 4. As recorded far infrared spectra of (a) undoped $GdBaCo_2O_{5.5}$ and (b) $GdBaCo_{1.6}Ni_{0.4}O_{5.5}$ for select temperatures spanning the T_{MIT}. Insets show the expanded view of the bending mode evolving across T_{MIT}.

an evident increase in the electronic absorption background is observed that points to a progressive increase in the density of the charge carriers. One can also see a systematic decrease in the phonon intensities accompanied by an evident broadening as the temperature is increased. For temperatures beyond T_{MIT} the phonon modes are observed to be totally smeared by the increased electronic absorption background, and the spectrum becomes totally featureless, signaling the transition to the delocalised state. Similar in situ variable temperature measurements were carried out on all the nickel doped samples $GdBaCo_{2-x}Ni_xO_{5.5}$ ($x=0.1$, $x=0.2$ and $x=0.4$) spanning the respective transition temperatures, to look for changes in the phonon modes across the transition. Fig. 4b shows a representative set of far infrared spectra of the $x=0.4$ sample—$GdBaCo_{1.6}Ni_{0.4}O_{5.5}$ in the temperature range 300–77 K spanning the T_{MIT} (~200 K). Since at room temperature this sample is metallic, the room temperature infrared spectrum is featureless and is seen to exhibit the characteristic metallic background. On lowering the temperature, not much of a change is observed until about 200 K. Interestingly for temperatures below 200 K the phonon modes are seen to gradually emerge from the absorption background signaling the transition to the insulating state. The emergence of the phonon modes at low temperatures can be understood as arising due to the decreased electronic absorption background in the insulating state.

3.4. Temperature dependence of the bending mode across T_{MIT}

Since it is well known [25] that changes in the bond angle between the octahedra Co1–O5–Co1 and the pyramids Co2–O4–Co2 and between the octahedra and the pyramids Co1–O6–Co2, would greatly influence the hopping probability of the charge carriers thus dictating the electronic properties of the system, it becomes important to follow the corresponding bending modes across the transition temperature. In the present work we have tried to analyze the most intense bending mode (350 cm^{-1}) of the CoO_6 octahedra/pyramids in detail—it is to be noted that this is the mode that involves major displacements of the Co1,Co2,O4 and O5 atoms (refer Table 3) that would help follow changes in both the octahedral and pyramidal bond angles. Inset of Fig. 4a shows the detailed evolution of the 350 cm^{-1} bending mode across the T_{MIT} for the undoped sample $GdBaCo_2O_{5.5}$. A noticeable reversal in the peak asymmetry is seen across the transition temperature, it is interesting to note that in the insulating state (~300 K), this mode exhibits a strong asymmetry towards the low frequency side after which the mode progressively becomes symmetric at ~360 K and later at the transition temperature (370 K) a sudden reversal in peak asymmetry towards the high frequency is observed. For temperatures beyond 400 K the mode is totally submerged by the increased electronic absorption background.

The detailed evolution of the bending mode of the $x=0.4$ sample across the T_{MIT} (300–77 K) (inset of Fig. 4b) clearly indicates the emergence of the phonon feature at 200 K. Although initially this mode exhibits an asymmetry towards the high frequency side, subsequently the mode tends to become symmetric as the temperature is lowered well within the insulating state.

In order to gain a further insight into the exact variation of the phonon line shape parameters in both undoped and nickel-doped $GdBaCo_2O_{5.5}$, detailed peakfit analysis of the 350 cm^{-1} bending mode of the CoO_6 octahedra were carried out to look for changes that could signal the insulator to metal transition. While attempts at fitting this mode to a Lorentzian/Gaussian in all these samples did not prove satisfactory, a Fano–Breit–Wigner line shape was seen to provide very good fits throughout the measured temperature range. This profile for a phonon mode is indicative of an enhanced interaction of this mode with a continuum of states [40]—in this case a continuum of free electrons characteristic of the delocalised state. This bending mode has hence been analysed in terms of a Fano–Breit–Wigner line shape

$$I = I_o\{1+[(\omega-\omega_o)/\Gamma q]\}^2/\{1+(\omega-\omega_o)^2/\Gamma^2\} \quad (1)$$

where the asymmetry factor '$1/q$' is a measure of the strength of the interactions of the phonon with a continuum of states.

The temperature dependency of the line shape parameters of this mode for the undoped and all the nickel-doped samples revealed anomalous changes that correlate well with the transition temperature (Fig. 5). From the figures one can also observe a clear indication of the suppression of the T_{MIT} with increasing nickel content.

3.4.1. Variation in phonon frequency across T_{MIT}

A sharp decrease in the bending mode frequencies on increasing the temperature, signals the transition to the delocalised state (Fig. 5a). A systematic suppression of the transition is also clearly evident with increased Ni content. The fact that the bending modes exhibit an abrupt softening at the insulator–metal transition can also be taken as definitive evidence of increased bond angles between the octahedra/pyramids thus suggesting delocalization of charge carriers along all directions on increasing the temperatures [25].

3.4.2. Variation of phonon line widths

Although regular anharmonic effects would cause increased phonon line widths on increasing the temperature, it is evident from Fig. 5b that the line widths exhibit a sudden and anomalous increase (over and above that expected for regular anharmonic behavior) that seems to correlate well with the T_{MIT}. This would

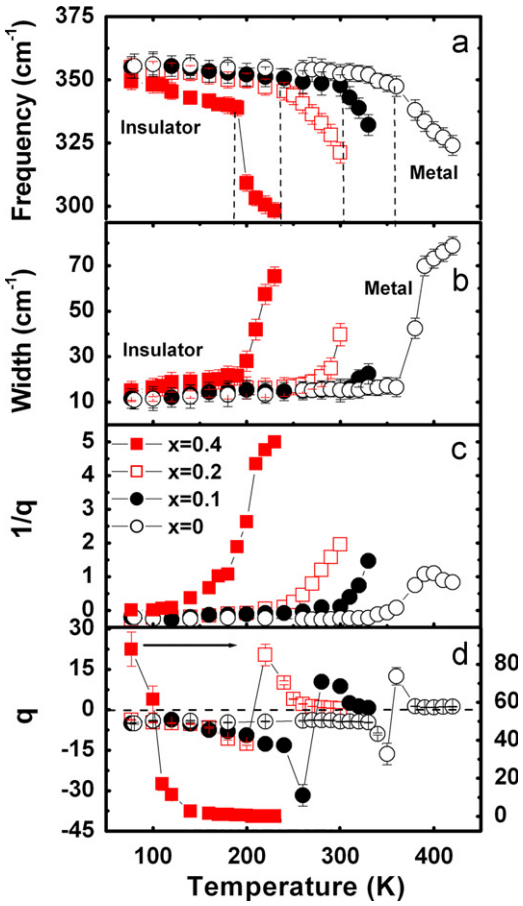

Fig. 5. Variation of the octahedral bending mode line shape parameters in $GdBaCo_{2-x}Ni_xO_{5.5}$ ($x=0$, 0.1, 0.2 and 0.4) as a function of temperature. The abrupt softening of the bending mode frequencies (a) the anomalous increase in phonon line widths (b) and the changes in asymmetry factors (c) and (d) are indicative of transition to the metallic state. Note the suppression of T_{MIT} with increased nickel contents.

imply an increased interaction of the phonon mode with a continuum of free electrons. [40].

Hence all the above signatures are clearly indicative of extensive electron–phonon interaction effects predominant in these systems [40]. It is well known that electron–phonon interactions are associated with the decay of a phonon into an electron–hole pair thus leading to the observed softening and broadening of the modes [41]. Additional support for the interaction of this mode with the free electrons in the medium is provided by the spectacular changes observed in both the variation of the asymmetry parameter '$1/q$' (Fig. 5c) and the Fano parameter 'q' (Fig. 5d) as the sample enters the high temperature phase.

A plot of the Fano parameter 'q' across the T_{MIT} for all the samples (except the 20% nickel doped sample) excellently reflects the reversal in peak asymmetry that correlates with the T_{MIT}. Although at present we are unable to attribute any particular reason for this reversal, nevertheless this reversal implies that in the insulating state the bending mode interacts with a continuum of electronic states with energies lower than its vibrational frequency, while above the transition temperature, the bending modes are observed to interact with a continuum of states having their energies centered at frequencies higher than the phonon frequency. The above observations clearly indicate that the phonons in these systems show correlated changes with the MIT providing direct evidence of the fact that the MIT in these systems are indeed driven by changes in structure.

3.5. Temperature dependence of the stretching modes in undoped $GdBaCo_2O_{5.5}$

Analysis of the variation in the stretch mode frequencies of the undoped sample was carried out across the T_{MIT} in an effort to see if the distortion effects of the octahedra would play a role in dictating this transition. In view of this, both the 503 mode and the 602 cm^{-1} mode corresponding to the stretching of the octahedra along the a–b plane and along the c-axis, respectively, (Table 3) have been analysed and the variation in mode frequencies across T_{MIT} have been plotted in Fig. 6a. The temperature dependencies of the octahedral stretching mode frequencies based on the cubic anharmonicity model [41] is given as follows:

$$\omega(T) = \omega(T)\text{-}\omega_0 = -A[(\exp(h/\omega_0/4\pi k_B T)-1)^{-1}+0.5] \quad (2)$$

The results obtained from the above model are shown as dotted lines in Fig. 6. While the 603 cm^{-1} mode exhibits extensive softening on increasing the temperature from 77 to 400 K over and above that expected for anharmonicity, the 503 cm^{-1} mode exhibits a sudden upturn in the mode frequencies at ~270 K after which the mode is seen to harden further with an evident change in slope at ~360 K signaling the MIT. We try to understand the above changes in the stretch mode frequencies as follows:

The anomalous softening exhibited by the 603 cm^{-1} 'c' axis stretch mode is in keeping with synchrotron diffraction measurements by Frontera et al. [13] wherein the Co–O bond lengths along the 'c' axis of both the pyramids and the octahedra are observed to increase across the transition.

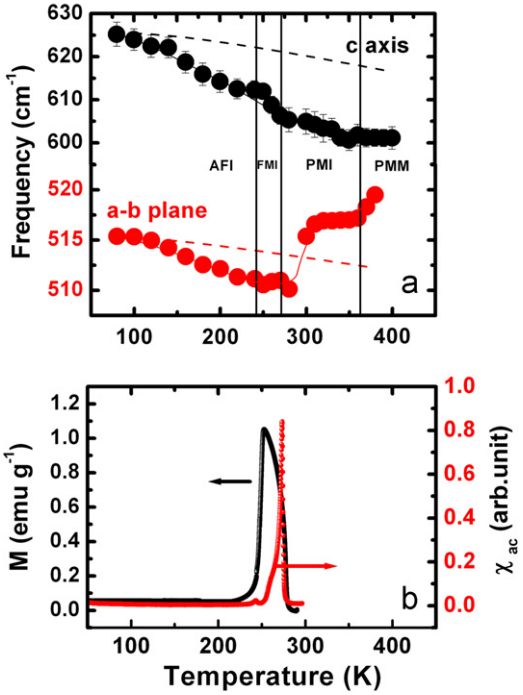

Fig. 6. Temperature dependence of (a) Co–O octahedral stretch mode frequencies, (b) magnetic susceptibility and magnetization across T_{MIT} in $GdBaCo_2O_{5.5}$. The octahedral stretch mode along the c-axis exhibits extensive softening while the stretching mode along the a–b plane exhibits a contraction on increasing the temperatures. The dotted lines correspond to the expected variation based on cubic anharmonicity. The vertical lines correspond to the various electronic and magnetic transitions of $GdBaCo_2O_{5.5}$. Note the correlation between the upturn of the stretch mode frequency along the a–b plane with the paramagnetic to ferromagnetic transition at 270 K.

Incidentally, the sudden change in slope of the 503 cm^{-1} feature (a–b stretch mode) at 270 K is seen to correlate well with the earlier reported magnetic transition wherein the system crosses over from the PM to the FM state on lowering the temperature [23] (Fig. 6). Although at present we are unable to provide any definitive reason for the above behavior, nevertheless correlated changes in phonon modes associated with magnetic transitions have also recently been reported in $BaFe_2As_2$ [42,43]. At temperatures beyond 360 K this mode is observed to harden further indicating a contraction along the a–b plane that correlates well with the MIT. These distortions could also be expected to modify the crystal field splitting energies, thus reducing the band gaps resulting in the observed transition.

4. Summary and conclusion

Far infrared absorption spectrum of the layered cobaltite $GdBaCo_2O_{5.5}$ has been recorded and preliminary mode assignments were carried out based on ab initio lattice dynamical calculations using the VASP simulation package. Doping the cobalt sublattice with increasing amounts of nickel indicates octahedral distortions that could modify crystal field splitting energies, resulting in the observed decreased resistivity. Infrared absorption measurements spanning the T_{MIT} in the undoped and the nickel-doped samples revealed definite signatures of extensive interactions of the bending mode of the CoO_6 octahedra with the changing electronic background. Dramatic softening of this mode on increasing the temperature indicates increased charge carrier delocalization. Clear indication of the suppression of T_{MIT} with increased nickel content has also been obtained. Temperature dependence of the octahedral stretch mode frequencies in $GdBaCo_2O_{5.5}$ point to distinct octahedral distortions accompanying the MIT, hinting at a structural origin of this high temperature transition.

References

[1] M. Zhuang, W. Zhang, N. Ming, Phys. Rev.B 57 (10) (1998) 705.
[2] S. Yamaguchi, Y. Okimoto, Y. Tokura, Phys. Rev. B 55 (1997) R8666.
[3] K. Asai, A. Yoneda, O. Yokokura, J.M. Trannquada, G. Shirane, K. Kohn, J. Phys. Soc. Jpn. 67 (1998) 290.
[4] H. Wu, J. Phys.: Condens. Matter 15 (2003) 503.
[5] Asish K. Kundu, P. Nordblad, C.N.R. Rao, Norbold, et al., J. Solid State Chem. 179 (2006) 923.
[6] Asish K. Kundu, K. Ramesha, Ram Seshadri, C.N. R Rao, J. Phys: Condens. Matter 16 (2004) 7955–7966.
[7] I.O. Troyanchuk, N.V. Kasper, D.D. Khalyavin, H. Szymczak, R. Szymczak, M. Baran, Phys. Rev. Lett. 80 (1998) 3380.
[8] T. Vogt, P.M. Woodward, P. Karen, B.A. Hunter, P. Henning, A.R. Moodenbaugh, Phys. Rev. Lett. 84 (2000) 2969.
[9] E. Suard, F. Fauth, V. Caignaert, I. Mirebeau, G. Baldinozzi, Phys. Rev. B 61 (2000) R11871.
[10] M. Respaud, C. Frontera, J.L. García-Muñoz, Miguel Angel G. Aranda, B. Raquet, J.M. Broto, H. Rakoto, M. Goiran, A. Llobet, J. Rodríguez-Carvajal, Phys. Rev. B 64 (2001) 214401.
[11] A. Maignan, C. Martin, D. Pelloquin, N. Nguyen, B. Raveau, J. Solid State Chem. 142 (1999) 247.
[12] Y. Moritomo, T. Akimoto, M.M. Takeo, A. Machida, E. Nshibori, M. Takata, M. Sakata, K. Ohoyamaand, A. Nakamura, Phys. Rev. B 61 (2000) R13325.
[13] C. Frontera, J.L. García-Muñoz, A. Llobet, M.A.G. Aranda, Phys. Rev. B 65 (2002) 180405 (R).
[14] A.A. Taskin, A.N. Lavrov, Yoichi Ando, Phys. Rev. B 71 (2005) 134414.
[15] A.A. Taskin, A.N. Lavrov, Y. Ando, Phys. Rev. Lett. 90 (2003) 227201.
[16] A.A. Taskin, Yoichi Ando, Phys. Rev. Lett. 95 (2005) 176603.
[17] F. Fauth, E. Suard, V. Caignaert, I. Mirebeau, Phys. Rev. B 66 (2002) 184421.
[18] A.A. Taskin, A.N. Lavrov, Y. Ando, Phys. Rev. B 73 (2006) 121101 (R).
[19] L. Ruiz- Gonzalez, K. Boulahya, M. Parras, Chem. Eur. J. 8 (2002) 5694.
[20] A.I. Klyndyuk, Inorganic Materials 45 (2009) 942 and references therein.
[21] C. Frontera, J.L. Garcia Munoz, A. Llobet, Li. Manosa, M.A.G. Aranda, J. Solid State Chem. 171 (2003) 349.
[22] S. Roy, M. Khan, Y.Q. Guo, J. Craig, N. Ali, Phys. Rev. B 65 (2002) 0644371.
[23] A. Bharathi, P. Yasodha, N. Gayathri, A.T. Satya, R. Nagendran, N. Thirumurugan, C.S. Sundar, Y. Hariharan, Phys. Rev. B 77 (2008) 085113.
[24] P. Yasodha, V. Sridhran, V. Srihari, A. Bharathi, V.S. Sastry, Y. Hariharan, C.S. Sundar, Proceedings of the Solid State Physics Symposium, vol. 51, 2008, pp. 719.
[25] E. Pomjakushina, K. Conder, V. Pomjakushin, Phys. Rev. B 73 (2006) 113105.
[26] K. Conder, E. Pomjakushina, V. Pomjakushin, M. Stingaciu, S. Streule, A. Podlesnyak, J. Phys.: Condens. Matter 17 (2005) 5815.
[27] L. Malavasi, M. Brunelli, Y.D. Fernandes, B. Pahari, P. Mustarelli, Phys. Rev. B 80 (2009) 153102.
[28] M. Lafkioti, E. Goering, S. Gold, G. Schutz, S.N. Barilo, S.V. Shiryaev, G.I. Bychkov, P. Lemmens, V. Hinkov, J. Deisenhofer, A. Loidl, New J. Phys. 10 (2008) 123030.
[29] J.B. Goodenough, et al., Phys. Rev. 124 (1961) 373;
R.T. Harley, Electron–phonon interaction and phase transitions, edited by T. Riste Plenum, New York, 1977, and references therein.
[30] S. Yamaguchi, Y. Okimoto, Y. Tokura, Phys. Rev. B 55 (1997) R8666.
[31] T. Saito, T. Arima, Y. Okimoto, Y. Tokura, J. Phys. Soc. Jpn. 69 (2000) 3525.
[32] K.H. Kim, J.Y. Gu, H.S. Choi, J.W. Park, T.W. Noh, Phys Rev Lett 77 (1998) 1877.
[33] M. Quijada, J. Ceme, J.R. Simpson, H.D. Drew, K.H. Ahn, A.J. Millis, R. Shreekala, R. Ramesh, M. Rajeswari, T. Venkatesan, Phys. Rev. B 58 (1998) 16093.
[34] M. Premila, T.N. Sairam, C.S. Sundar, Curr. Sci. 88 (2005) 102.
[35] Yu.G. Pashkevich, V.P. Gnezdilov, P. Lemmens, K.K. Choi, K.V. Lamonova, A.A. Gusev, G. Guntherodt, S.N. Barilo, S.V. Shiryaev, G.L. Bychkov, in: Eric C. Faulques, Dale L. Perry, V. Andrei Yeremenko (Eds.), Spectroscopy of emerging Materials, 165, Kluwer Academic publishers2004, p. 195.
[36] G. Kresse, J. Hafner, Phys. Rev. B 47 (1993) 558; See also G. Kresse and J. Furthmüller, Phys. Rev. B 54 (1996) 11169. For details about the package, see 〈http://cms.mpi.univie.ac.at/vasp/vasp/vasp.html〉.
[37] J.P. Perdew, K. Burke, M. Ernzerhof, Phys. Rev. Lett. 77 (1996) 3865.
[38] G. Kresse, D. Joubert, Phys. Rev. B 59 (1999) 1758.
[39] R. Rajaraman et al., to be communicated.
[40] U. Fano, Phys. Rev. 124 (1961) 1866.
[41] P.B. Allen, Solid State Commun. 14 (1974) 937.
[42] Taner Yildirim, Physica C 469 (2009) 425.
[43] A. Akrap, J.J. Tu, L.J. Li, G.H. Cao, Z.A. Xu, C.C. Homes, Phys. Rev. B 80 (2009) 180502 R.